Wideband Time- and Frequency-Domain EMI: Phenomenology and Signal Processing

Lawrence Carin
Electrical and Computer Engineering Department
Duke University

I.J. Won and Dean Keiswetter
Geophex, Ltd.
Raleigh, NC

Carl E. Baum
Air Force Research Laboratory
Directed Energy Directorate

Abstract

The phenomenology of frequency- and time-domain electromagnetic induction (EMI) is examined in detail, through use of a rigorous electromagnetic scattering model, and through appropriate signal analysis. Particular attention is placed on the potential of the new GEM-3 sensor, an EMI device developed by Geophex, Ltd. for very wideband EMI operation. We demonstrate that both the time- and frequency-domain EMI signatures can be characterized in terms of a few magnetic singularities, thereby significantly reducing the number of features that need be stored for target identification. Further, we examine the aspect-dependent properties of the relative excitation strengths of the magnetic-singularity modes. Finally, we perform a statistical analysis of the relative efficacy of frequency- and time-domain EMI operation, for a class of conducting targets.

AFRL/DE 99-27

Geophex, Ltd.
605 Mercury Street
Raleigh, NC 27603-2343
Tel: (919) 839-8515
Fax: (919) 839-8528

AFRL/DEPH
Attn: Mr. Robert Torres, AFRL/DEHP   Phone (505) 846-0296
3550 Aberdeen Avenue SE
Kirtland AFB NM 87117-5776

Dear Mr. Torres:

I would like to submit for public release the attached paper that will be submitted as
an Interaction Note. The paper is entitled "Wideband Time- and Frequency-domain
EMI: Phenomenology and Signal Processing." This paper was written under funding
of contract #F29601-98-C-0154, entitled "Broadband Electromagnetic Sensing for
Weapons Detection." There is no company proprietary data in this Note.

If you have any questions, please do not hesitate to call me directly at (919) 839-
8515.

Sincerely,

Dean Keiswetter, Ph.D.
Program Manager

AFRL/DE 99-27

Wideband Time- and Frequency-Domain EMI: Phenomenology and Signal Processing

Lawrence Carin
Electrical and Computer Engineering Department
Duke University

I.J. Won and Dean Keiswetter
Geophex, Ltd.
Raleigh, NC

Carl E. Baum
Air Force Research Laboratory
Directed Energy Directorate

Abstract

The phenomenology of frequency- and time-domain electromagnetic induction (EMI) is examined in detail, through use of a rigorous electromagnetic scattering model, and through appropriate signal analysis. Particular attention is placed on the potential of the new GEM-3 sensor, an EMI device developed by Geophex, Ltd. for very wideband EMI operation. We demonstrate that both the time- and frequency-domain EMI signatures can be characterized in terms of a few magnetic singularities, *thereby significantly reducing the number of features that need be stored for target identification.* Further, we examine the aspect-dependent properties of the relative excitation strengths of the magnetic-singularity modes. Finally, we perform a statistical analysis of the relative efficacy of frequency- and time-domain EMI operation, for a class of conducting targets.

1

Contents

I. Introduction

It is well known that finite dielectric objects composed of a large dielectric contrast relative to the background medium (air) generally support high-Q electromagnetic resonances [1]. This concept is exploited in the design of microwave filters. If the dielectric resonator has a wavenumber $k=\omega[\mu\varepsilon]^{1/2}$, where ω is the real angular frequency and μ and ε are the resonator permeability and permittivity, respectively, the electric fields inside the resonant structure satisfy the source-free wave equation

$$\nabla^2 E + k^2 E = 0 \qquad\qquad (1)$$

with appropriate boundary conditions. For low-loss dielectric resonators, the resonant frequency ω is nearly purely real, manifesting the aforementioned high-Q resonances [1]. We use these well-known properties of dielectric resonators to address the electromagnetic induction (EMI) resonances of highly conducting and possibly permeable targets (at kilohertz frequencies) [2-5].

For a material with conductivity σ, the effective dielectric constant satisfies $\varepsilon=\varepsilon_o-j\sigma/\omega$, where $j\equiv(-1)^{1/2}$. For the very good conductors of interest, $\sigma >> 1$ and $\varepsilon\approx-j\sigma/\omega$. The associated wavenumber $k=\omega[-j\mu\sigma/\omega]^{1/2}$ and $k^2=-j\mu\sigma\omega$. We note that if $\omega=j\omega_i$, then k^2 is purely real as in (1), and therefore the dielectric-resonator theory appropriate for low-loss dielectrics at real frequencies will be appropriate here for highly conducting (and possibly ferrous) targets, at purely imaginary resonant frequencies. Moreover, the modal structure of the dielectric-resonator modes at real frequencies will be analogous to those expected for the EMI resonant modes of highly conducting targets, where in the latter case the resonant frequencies are purely imaginary.

As for the dielectric resonator [1], a highly conducting EMI resonator will support an infinite number of modes [2]. In the dielectric-resonator case the number of modes excited is dictated by the system bandwidth, since the resonant frequencies are nearly purely real. For the EMI case we need be more careful, since the resonant frequencies are purely imaginary, and therefore the connection

to real frequencies is less obvious. The resonant frequencies correspond to first-order poles in the complex frequency plane [2,4,5], and therefore we can express the target transfer function as

$$H(\omega) = a + \sum_n \frac{b_n \omega}{\omega - j\omega_n} \qquad (2)$$

where ω_n corresponds to the magnitude of the nth pole. Equation (2) is valid at EMI frequencies, characterized by an operating wavelength that is very large relative to representative target dimensions. Note in the limit $\omega \to 0$, $H(\omega) \to a$. Therefore, $a=0$ for nonferrous targets; this feature may be useful as a discriminant.

Note the ω in the numerator of the terms summed in (2) (see also [5]). This is motivated by the high-frequency EMI limit at which the skin depth is small relative to principal target dimensions. At such frequencies minimal frequency variation is expected. Hence, this term is motivated by the high-frequency limit, while a is dictated by the low-frequency regime. We will also see that the ω in the numerators in (2) will also play an important role in yielding the expected real impulse response. In particular, to find the step response, we convert (2) to the time domain via the inverse Fourier transform and, using residue calculus, we have

$$h(t) = \frac{1}{2\pi} \int_{-\infty}^{\infty} \frac{H(\omega)}{j\omega} e^{j\omega t} d\omega = au(t) + \sum_n u(t) b_n e^{-\omega_n t} \qquad (3)$$

where u(t) represents the usual step function. We note that the expression to the right of (3) is actually an approximation to the impulse response, valid over EMI frequencies, because the H(ω) to the left is integrated over all frequencies in the Fourier transform (including those for which (2) is invalid). Within these approximations, the EMI impulse response is represented by a sum of damped exponentials for nonferrous targets, each representative of an L-R circuit. For ferrous targets, we

4

have the additional $a\delta(t)$.

Returning to the transfer function in (2), we note that the real and imaginary parts of the nth term in the sum are equal at the *real* frequency $\omega=\omega_n$ [5]. As will be demonstrated when presenting results, frequency-domain EMI operation is most effective around such frequencies, these representing regions for which the in-phase (I) and quadrature (Q) portions of the EMI response are particularly target dependent.

II. Approximate EMI Resonances of Simple Shapes

As discussed in motivating (2), EMI resonances at imaginary frequencies are analogous to dielectric-resonator resonances at real frequencies. While there are rigorous analyses available for computing the resonances of dielectric resonators [1], there are simple back-of-the-envelop calculations one can perform to yield approximate solutions for the resonant frequency. Likewise, for the EMI case [6] we have developed a rigorous numerical model for computing imaginary EMI resonances. However, we first consider a solution for a simple but important class of shapes, which will yield approximate solutions and physical insight. Consider a cylinder of radius r and height h, composed of material with conductivity σ and permeability μ. We can analyze the resonant modes of this structure by imposing the boundary condition that the component of electric field normal to the target walls must vanish, constituting what is often termed a perfectly magnetic wall (tangential magnetic fields equal to zero). This technique is well known for the approximate analysis of dielectric resonators [1]. Such a structure supports modes with electric fields transverse to z (TE$_z$) and magnetic fields transverse to z (TM$_z$), where z is along the target axis.

For TE$_z$ modes we have the condition [7]

$$k = \sqrt{\omega_i \mu\sigma} = \sqrt{(\chi_{mn}/r)^2 + (p\pi/h)^2} \qquad (4)$$

5

with $m=0, 1, 2, ...; n=1, 2, 3, ...;$ and $p=0, 1, 2, ... $. For TM$_z$ modes we analogously have

$$k = \sqrt{\omega_i \mu \sigma} = \sqrt{(\chi'_{mn}/r)^2 + (p\pi/h)^2} \qquad (5)$$

where $m=0, 1, 2, ...; n=1, 2, 3, ...;$ and $p=1, 1, 2, ... $. The expressions χ_{mn} and χ'_{mn} represent the nth roots of $J_m(\cdot)$ and $J_m'(\cdot)$, respectively, where $J_m(\cdot)$ is the Bessel function [7]. If the currents on the target have no azimuthal variation, we consider $m=0$ modes, and therefore only TE$_z$ modes are excited. Moreover, if we assume no variation along the z direction (*i.e.*, only variation in the radial direction), then the imaginary resonant frequencies are approximately

$$\omega_n \approx [\frac{\chi_{0n}}{r}]^2 \frac{1}{\mu\sigma} \quad , n = 1, 2, ... \qquad (6)$$

We note that, for a fixed target size, the resonant frequencies scale simply with changing σ and μ. This analysis can be used to quantify the approximate imaginary resonant frequencies of such things as firing pins (a similar analysis can be applied for hollow cylinders), from which one can estimate the expected decay constants (see (3)) or regions where the I and Q components of the frequency-domain EMI response are expected to be equal (see paragraph just prior to Sec. II).

III. Method of Moments Analysis

A. General construct

While Sec. II has discussed an approximate method for the analysis of an important target class, in general numerical algorithms are required for more-general targets. Here we have employed a surface-integral equation formulation, in which boundary conditions are rigorously imposed on the

target surface. The tangential electric and magnetic fields on the surface are expanded in a known basis with unknown basis-function coefficients, the latter solved for by transforming the continuous integral equations into matrix form, using a Galerkin testing procedure [8]. For N basis functions, we arrive at the equation $\mathbf{Zi=v}$, where $\mathbf{i}$ is an N-dimensional vector representing the basis-function coefficients to be determined, $\mathbf{v}$ is an N-dimensional vector representing the excitation fields at the positions of the basis function, and $\mathbf{Z}$ is an $N{\times}N$ matrix representing interaction between the N expansion functions. Once the currents $\mathbf{i}$ are determined, the scattered fields are readily computed.

As discussed in Sec. I, the modes of the system correspond to poles of the transfer function. Consequently, these poles can be computed by determining the frequencies at which the frequency-dependent matrix $\mathbf{Z}$ is singular, or those frequencies for which the determinant of $\mathbf{Z}(\omega)$ vanishes. This can also be recognized by the fact that these poles represent the natural (non-driven) response of the target, for which $\mathbf{Zi}{=}0$. To obtain nontrivial solutions for $\mathbf{i}$ we require the determinant of $\mathbf{Z}$ to vanish.

We have developed a method of moments algorithm for scattering from a general conducting, permeable body of revolution (a target with rotational symmetry). Many man-made targets of interest satisfy this model. Further, we have implemented the excitation $\mathbf{v}$ such that it corresponds to the fields excited by the Geophex GEM-3 [9].

B. Surface integral equation and method-of-moments

We consider electromagnetic scattering from highly (but not perfectly) conducting and permeable targets situated in a homogeneous environment, *e.g.* free space. Moreover, we specialize the solution to the case of a body of revolution (BOR). Because the surface integral equation approach for treating problems involving perfectly conducting as well as low-loss dielectric BORs has been studied by various authors [10-19] only a brief summary of the basic theory will be given here.
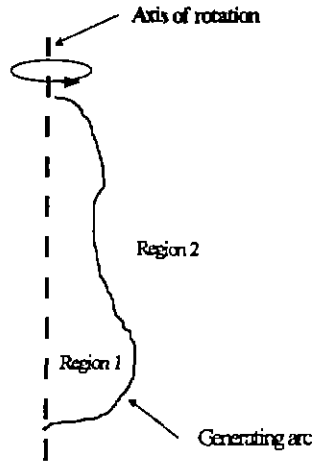
Figure 1. Body-of-revolution (BOR) model used to characterize scattering from and the resonances of a general conducting and ferrous target.

Considering Fig. 1, region 1 and region 2 are characterized by (possibly frequency dependent) medium parameters $(\varepsilon_1, \mu_1, \sigma_1)$ and $(\varepsilon_2, \mu_2, \sigma_2)$, respectively. According to surface equivalence principles [7], exterior scattered fields (E^{scat}, H^{scat}) and interior total fields (E, H) may be determined from a set of equivalent electric and magnetic surface currents. These equivalent surface currents are related to the total tangential magnetic and electric field by $J_s = \pm \hat{n} \times H$ and $M_s = \pm E \times \hat{n}$, respectively, where the upper sign holds for the exterior and the lower sign for the interior region. Coupled integral equations

$$E_{\text{tan}}^{inc}(r) = \Re_{EJ} J_s + \Re_{EM} M_s = \left[\sum_{i=1}^{2} \left(j\omega A_i(r) + \nabla \Phi_{ei}(r) \right) \right]_{\text{tan}} + \left[\nabla \times \sum_{i=1}^{2} \frac{F_i(r)}{\sigma_i + j\omega \varepsilon_i} \right]_{\text{tan}} \quad (7a)$$

8

$$H_{\text{tan}}^{inc}(r) = \Re_{HJ}J_s + \Re_{HM}M_s = \left[-\nabla \times \sum_{i=1}^{2}\frac{A_i(r)}{\mu_i}\right]_{\text{tan}} + \left[\sum_{i=1}^{2}\left(j\omega F_i(r) + \nabla \Phi_{mi}(r)\right)\right]_{\text{tan}} \quad (7b)$$

for the surface currents are obtained by satisfying the boundary conditions at the interface [14-19], where $(E_{\text{tan}}^{inc}, H_{\text{tan}}^{inc})$ represent the tangential components of the incident field. Herein the electric and magnetic vector and scalar potentials are defined as follows [7]

$$A_i(r) = \mu_i \oiint_{S'} G_i(r,r')\, J_s(r')dS' \quad (8a)$$

$$F_i(r) = \frac{\sigma_i + j\omega\varepsilon_i}{j\omega} \oiint_{S'} G_i(r,r') M_s(r')dS' \quad (8b)$$

$$\Phi_{ei}(r) = \frac{j\omega}{\sigma_i + j\omega\varepsilon_i} \oiint_{S'} G_i(r,r')\, q_{es}(r')dS' = \frac{-1}{\sigma_i + j\omega\varepsilon_i} \oiint_{S'} G_i(r,r') \nabla' \cdot J_s(r')dS' \quad (9a)$$

$$\Phi_{mi}(r) = \frac{1}{\mu_i} \oiint_{S'} G_i(r,r') q_{ms}(r')dS' = \frac{-1}{j\omega\mu_i} \oiint_{S'} G_i(r,r') \nabla' \cdot M_s(r')dS' \quad (9b)$$

with the Green's function

$$G_i(r,r') = \frac{e^{-jk_i|r-r'|}}{4\pi|r-r'|} \quad \text{with} \quad k_i = \sqrt{\omega^2\varepsilon_i\mu_i - j\omega\mu_i\sigma_i} \quad \text{and} \quad i = 1,2 \quad (10)$$

for the homogeneous interior ($i=1$) and homogeneous exterior ($i=2$) region, respectively. The complex wave numbers of the interior and exterior region are given by k_1 and k_2, and the vectors r and r' represent source and observation point, respectively.

Equations (7-10) are valid for an arbitrarily shaped homogeneous target in a homogeneous environment, for which a Method-of-Moments (MoM) solution could be applied [14-19]. However, we only consider the special case of a BOR (Fig. 1), which is formed by rotating a generating arc

about an axis that is chosen to be the z-axis of a Cartesian coordinate system [10-19]. For numerical simulations, the generating arc is approximated by a sequence of linear segments. Coordinates (ϕ, t) are introduced, where the angle ϕ is equal to the one used in cylindrical coordinates (ρ, ϕ, z) and t is the length variable along the curve generating the arc. To take advantage of the rotational symmetry, the incident field, all currents and scalar Green's functions are expanded into discrete Fourier series, by taking a Fourier transform in the azimuthal (ϕ) direction, from which the general solution reduces to an infinite number of distinct MoM problems for each of the Fourier modes (each with azimuthal variation $\exp(jm\phi)$). The resulting sets of simultaneous equations may be represented in matrix form as

$$\left[Z^m \right] I^m = V^m \quad \text{for} \quad m = 0, \pm 1, \pm 2, \pm 3, \dots \tag{11}$$

where $[Z^m]$ is the moment matrix, I^m is a column vector containing the unknown basis function coefficients, and V^m is the driving vector for the mth Fourier mode [10-19]. Details regarding the calculation of the impedance matrix or the driving vector can be found in the literature.

If we are interested in the natural resonances of the target, the driving vector V^m is set to zero. Then the system (11) of linear equations has a non-trivial solution only if the determinant of the MoM impedance matrix is zero:

$$\det \left[Z^m (s_{m,v} = j\omega_{m,v}) \right] = 0 \quad \text{with} \quad s_{m,v} = j\omega_{m,v} = j[\omega'_{m,v} + j\omega''_{m,v}] = -\omega''_{m,v} + j\omega'_{m,v} \tag{12}$$

The roots of (12) in the complex frequency plane are the resonant frequencies of the modes (m,v). Searching for these complex roots is relatively easy because, for highly conducting and permeable targets, the real part is much smaller than the imaginary part (almost pure exponential damping, as expected from Sec. I). Thus it is best to search first along the imaginary frequency axis for an approximate solution, after which Mueller's method is performed to yield an accurate solution for the complex resonant frequency (where we have found 5 to 10 iterative steps generally sufficient).

For mode identification, it is principle necessary to compute the detailed field distribution inside and outside the target. But, in a limited sense, this may be accomplished by studying the resonant

10

surface current distribution only. For each complex resonant frequency the surface currents, or, equivalently, the tangential fields along the surface, can be readily calculated.

In contrast to MoM calculations for perfectly conducting objects [13], for which subsectional basis-function discretization only depends on the wavelength in the outside region (often free-space), the maximum subsection length here has to be chosen with respect to the wave number inside the highly conducting and permeable object. Neglecting displacement currents and assuming a real permeability μ_1, this wave number is given by

$$k_1 = k_1' - jk_1'' = \sqrt{\frac{\sigma_1 \mu_1}{2}} \left(\sqrt{|\omega| + \omega''} - j\sqrt{|\omega| - \omega''} \right) . \tag{13}$$

Reasonable results are obtained if the subsection length Δt (along the generating arc) satisfies the conditions $k_1' \Delta t \leq 2\pi/10$ and $k_1'' \Delta t \leq 1/2$, which means at least 10 subsections per wavelength and at least two per skin depth.

IV. Frequency and Time-Domain Target Identification

A. Frequency domain

Assume that the GEM-3 [9] is used to measure the $2M$ dimensional vector g, representing the I and Q (real and imaginary part of frequency-domain response, respectively) at M frequencies. Further, assume that $g=s+n$, where s represents the response of the target itself, and n represents system noise. The optimal detector is effected as [20]

11

$$\frac{p_n(g-s)}{p_n(g)} \quad \overset{\text{Target}}{\underset{\text{No Target}}{\overset{>}{\underset{<}{\quad}}}} \quad T \qquad (14)$$

where $p_n(\cdot)$ represents the known noise probability density function and s is also assumed known. If the ratio is larger than the threshold T, the target characteristic of waveform s is declared present. Otherwise, the target characteristic of s is declared not present. In principle, one must store the frequency dependent signature s for all targets, all frequencies of interest, and all target-sensor orientations. This latter condition makes this paradigm impractical.

We can make use of (2) to ameliorate this problem. The first important insight to recognize is that the resonant frequencies $j\omega_n$ are independent of the target-sensor position, with the variation in such handled by a and the mode coefficients b_n. If these terms are contained in the vector c, we have a parametric representation for the target signature, denoted $s(c)$, where we have exploited the expression in (2). A generalized likelihood-ratio test (GLRT) [20] is given by finding the c that maximizes $p_n[g-s(c)]$, for given measured data g. The expression in (14) is generalized to

$$\frac{\underset{c}{\max} \; p_n[g-s(c)]}{p_n(g)} \quad \overset{\text{Target}}{\underset{\text{No Target}}{\overset{>}{\underset{<}{\quad}}}} \quad T \qquad (15)$$

The receiver operating characteristic (ROC) [20] is determined by adjusting the threshold T, characterizing the probability of detection versus the probability of false alarm.

Therefore, the GLRT is effected by developing a library containing the relatively few aspect-dependent resonant frequencies characteristic of the targets of interest. From (15), we find the parameters c from (2) that maximize the GLRT. If multiple targets are to be distinguished, the target that yields the highest ratio in (15) is declared the target present; if none of the library of modal poles

12

yield a likelihood ratio that is above a prescribed threshold T, the putative target is declared clutter. Finally, for the case for which n is white Gaussian noise, the ratio in (15) reduces to a matched filter.

From the discussion in Sec. I, it is recognized that the targets are distinct at and around frequencies for which I and Q are equal, this frequency being target dependent and thereby aiding discrimination. In the subsequent results, this is illustrated for several targets. An EMI sensor will typically operate in the 0.1-100 KHz frequency band [9], and therefore this scheme is best for targets characterized by principal resonant modes with frequencies ω_n in this band. This is likely to be possible for nonferrous targets. However, from (6), we see that for highly ferrous targets (*e.g.*, iron has $\mu_r=5000$) the lowest frequencies (small modal order n) are at $\omega_n < 1$, for most realistically sized targets. Therefore, the frequency at which I and Q cross is less than 1 Hz and therefore of little value for a realistic frequency-domain EMI system. However, from (3), recall that the resonant fields decay as $\exp(-\omega_n t)$ in the time domain. Therefore, for situations in which ω_n is very small and therefore the target is less attractive for a frequency-domain EMI system, the time-domain response will decay slowly. It is for such situations that time-domain operation may be preferable.

It is interesting to note that frequency- and time-domain EMI operation are complementary. When $\exp(-\omega_n t)$ decays quickly, the cross-over frequency for I and Q is likely within the bandwidth of most frequency-domain EMI systems. However, when ω_n is too small to be in the bandwidth of most EMI systems (*e.g.*, large ferrous targets), the decay constant is likely to be sufficiently small, such that it can be readily extracted from a time-domain system.

B. Time domain

Consider equation (6), which gives some feel for the imaginary resonant frequency of the lowest cylindrical-target mode. We consider this structure in the example results. The lowest-order mode is characterized by $\chi_{01}=2.4049$. Consider a 1 inch diameter cylinder of 1 inch height. Aluminum and stainless-steel targets are nonferrous, and are characterized by $\sigma=3\times10^7$ S/m and $\sigma=1.3\times10^6$ S/m, which from (6) yield lowest-order resonances at j151 and j3493, respectively. From the discussion

in Sec. I, the I and Q of the frequency-domain EMI responses of these targets will cross in the vicinity of the real frequencies 151 Hz and 3493 Hz, respectively, defining regions where the EMI response is particularly target dependent and therefore salutary for discrimination. We also note that the predictions from (6) are slightly smaller than the method-of-moments computed resonant frequencies, but that (6) does yield an accurate approximation to the frequency bands of interest.

Now consider a target of the same shape as addressed above, but composed of nickel ($\sigma=3\times10^7$ S/m and $\mu_r=600$ H/m). From (6), the corresponding lowest order resonance is at j0.25 and consequently theoretically I and Q cross in the vicinity of the real frequency 0.25 Hz. It is unlikely that a frequency-domain EMI system can be designed to operate at such frequencies. From (6), we see that this issue is exacerbated as the target size is increased.

It is interesting to note that this problem is manifested by the small size of ω_n (see (3)). However, as discussed above, for small ω_n the time-domain EMI response decays very slowly, propitious conditions for the accurate extraction of decay constants from time-domain data. These decay constants are aspect independent, as they are characteristic of the target natural modes (resonances), and this therefore represents an alternative tool for target identification. On the other hand, when ω_n is large, as in the aforementioned nonferrous targets, the exponentials in (3) decay very quickly, making the extraction of decay constants far more susceptible to noise. Fortunately, as mentioned, the large ω_n are appropriate for wideband frequency-domain operation, in the manner discussed above an displayed in the results.

The decay constants can be extracted by using a class of parametric signal processing algorithms [6], often termed "superresolution" schemes [21].

V. Example Phenomenological Results

A. Characteristics of frequency-domain and time-domain EMI

We demonstrate the utility of the MoM analysis in Figs. 2 and 3, where we plot the log of the determinant of the MoM matrix [6], as a function of imaginary frequency. Theoretically, the resonant frequencies exist at frequencies for which the determinant vanishes. Numerically, it is not possible for the determinant to vanish exactly, since we utilize a finite set of basis functions to represent the generally continuous current distribution on the target surface (however, this problem could be mitigated by making appropriate approximations to the integral equation [3]). However, we have found empirically that sharp nulls in the frequency-dependent determinant occur at the appropriate
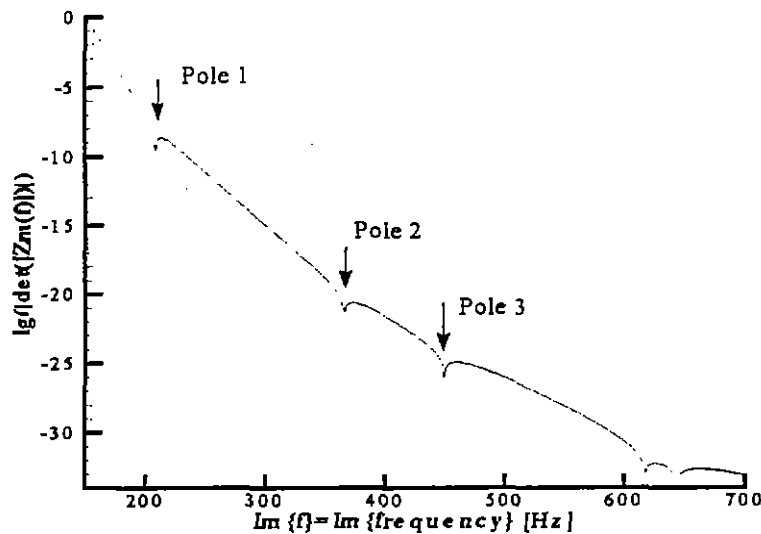
resonant frequencies. In Figs. 2 and 3 we consider conducting cylinders of 1 inch height and 1 inch diameter, for aluminum **Figure 2.** Determinant of the MoM impedance matrix Z, plotted as a function of the imaginary frequency. The marked sharp nulls correspond to the resonant modes of the target. Results are shown for the $m=0$ case, implying no azimuthal variation.
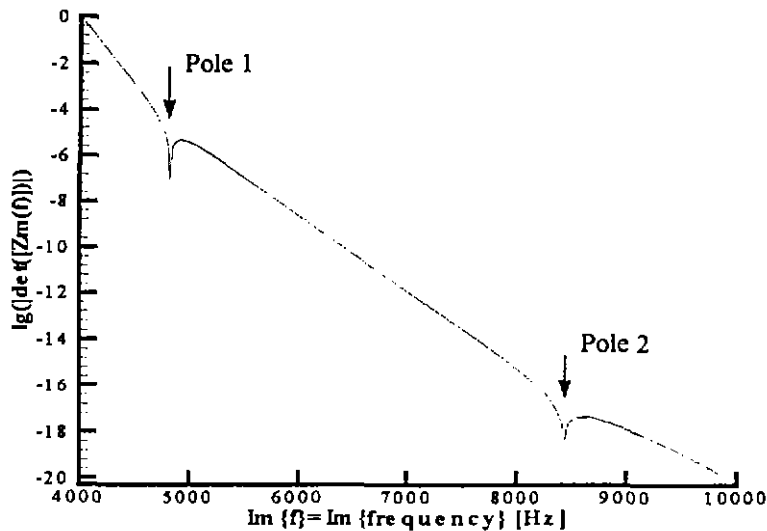
15

Figure 3. As in Fig. 2, but for a stainless-steel target.

and stainless-steel targets, respectively. In these computations we have considered the m=0 resonant mode, which corresponds to the case for which the fields have no azimuthal variation. For the relatively small targets of interest here, these are the principal modes of interest.

A couple of comments are in order concerning Figs 2 and 3. From the standpoint of a radar-based system, it would be impossible to distinguish these two targets, for each would appear as a perfect conductor with identical shape. However, we see that, despite the fact that these targets have identical shapes, they are clearly distinguished by their EMI, imaginary resonant frequencies. Secondly, recall from (2) that, in the case of exciting a single resonance, the I and Q components are equal at a frequency corresponding to the magnitude of the imaginary resonant frequency [5]. For the practical case of multi-mode excitation, things are complicated further, but the general phenomenon still applies. From Fig. 2 we see that the principal resonant frequency of the aluminum target is at approximately 200 Hz, while this occurs at approximately 4500 Hz for the stainless-steel target. These two frequencies are clearly quite different and therefore suggest that there is significant potential for EMI discrimination through exploitation of the disparate frequency-domain EMI signature. Further, we note that these "cross-over" frequencies are well inside the frequency band of the GEM-3 sensor [9], and therefore this feature can be exploited in practice.
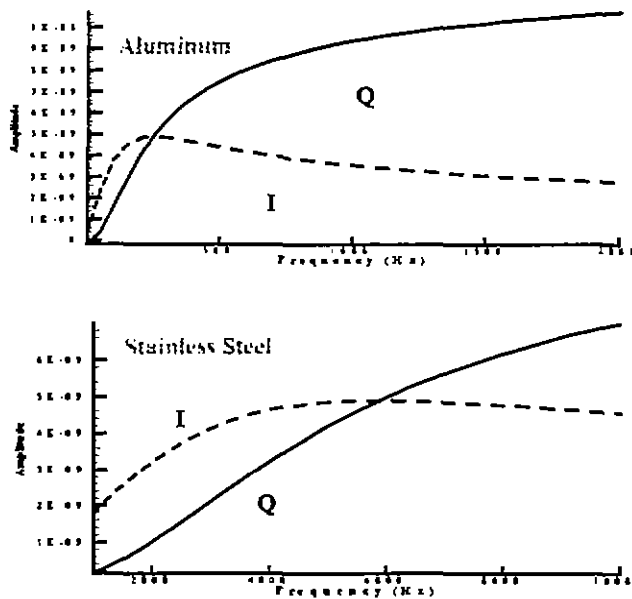
16

Figure 4. In-phase (I) and quadrature (Q) components of the magnetic field, computed via our MoM analysis, for the details of the GEM-3 sensor. Results are plotted for the aluminum and stainless steel target considered in Figs. 2 and 3, respectively. These data represent the GEM-3 data divided by $j\omega$.

In Fig. 4 we plot the MoM-computed GEM-3 response, as a function of *real* frequency. We see that, as predicted above, the I and Q responses cross approximately at the magnitude of the fundamental resonant frequency. Consequently, the frequency-dependent EMI-responses of these targets are markedly different.

Above we have concentrated on frequency-domain EMI operation. Alternatively, one can seek to exploit the resonant frequencies in the time domain, through use of (3). From (3), we see that the time-domain EMI response from a target is characterized by a sum of exponentially damped waveforms, and the rate of decay is given by $\exp(-\omega_n t)$, where ω_n is the magnitude of the resonant frequency for the nth mode. However, we note that the initial portion of the transient EMI response will be a replica of the incident waveform, *followed* thereafter by the exponentially damped tail. If the nominal temporal support of the incident waveform is T, with T dictated by the system bandwidth, then we can only attempt to extract ω_n for time $t > T$. We consider the 1-inch diameter, 1-inch high stainless-steel cylinder addressed above. That target has a principal resonance for ω_n approximately equal to 4500 Hz, with a corresponding 1/e time of 0.222 ms. This consequently places constraints

17

on a transient system, such that it is fast enough to measure the exponential resonant decay, before it is buried in the system noise. For example, a system with 100 KHz bandwidth can generate a transient excitation of T=0.01 ms duration, short enough such that exponential decay is of appreciable amplitude for t>T. For example, in Fig. 5 we plot the exponentially damped response of the stainless-steel for t>T, when a transient excitation is considered with bandwidth extending from 0.5-100 KHz. For computation of these results, we utilized our frequency-domain MoM algorithm [6], followed by an FFT to synthesize the time-domain scattered waveform.
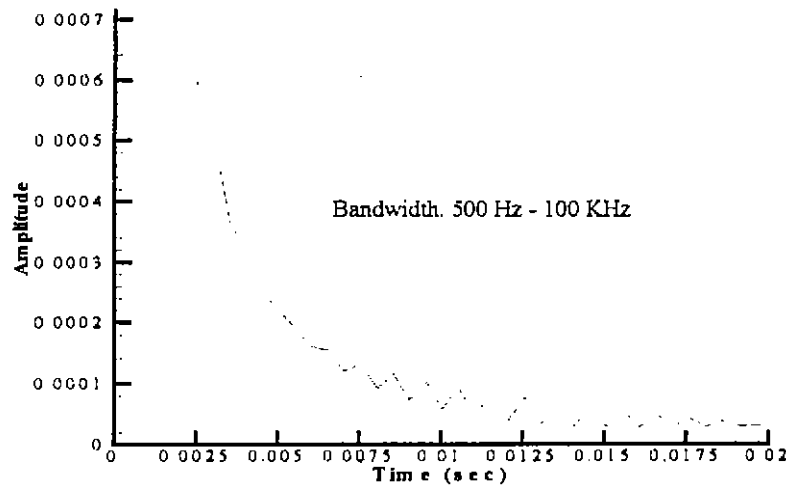

Figure 5. Exponentially damped response of a stainless-steel cylinder, due to excitation with a 100 KHz bandwidth pulse. Results are only plotted in the exponentially damped tail of the scattered response, after the early-time (t<T) response has been windowed out. The results were computed via the MoM, for the geometry of the GEM-3 sensor [9].

Before proceeding, it is important to distinguish the results in Figs. 4 and 5. While both of these results exploit the EMI resonances, they do so in very different ways. In Fig. 4 we considered frequency-domain EMI operation, and therefore we utilize the entire EMI response. In Fig. 5 we

18

consider time-domain EMI operation, and therefore the resonant response can only be exploited at late times, t>T. Consequently, for time-domain operation we have two drawbacks. First, we discard all time-domain information for t<T (early-time information), while in the frequency-domain approach we utilize all the measured information. Secondly, for a time-domain system we require sufficient bandwidth (small T) such that the signal extracted for t>T is of sufficient amplitude as not to be corrupted by noise. For frequency-domain operation we have no such bandwidth restrictions, other than designing the system such that it operates over the salutary frequencies over which the I and Q cross (Fig. 4), for the targets of interest.

We note in this context that there is an analogue between a time- and frequency-domain EMI system. In particular, as discussed above, a time-domain system requires a large span of frequencies to enhance noise immunity (*i.e.*, to reduce T). A frequency-domain system, on the other hand, benefits from averaging over extended time, to reduce system noise.

B. Single and multi-pole expansions

In the generalized-likelihood ratio test (GLRT) [20] in (15), we project a library of signals onto the measured signal, and determine the parameters that maximize the likelihood test. Here we utilize the frequency-domain response of the target-dependent resonant modes as the library of constituent features to which we match the signal under test. From (2), assuming non-ferrous targets ($a=0$), each resonant mode's frequency-dependent response is determined uniquely in terms of its associated resonant frequency ω_n. We assume that the set of resonant frequencies characteristic of a given target have been computed, as above, or are known from measurement. Consequently, in the context of a GLRT, we must determine the modal amplitudes that best match the data under test, *i.e.*, the coefficients b_n in (2). If the noise is additive, Gaussian, and uncorrelated, then the maximum-likelihood (ML) estimation [20] of the parameters b_n is characterized by a least-squares fit.

In Figs. 6 and 7 we consider EMI data computed via MoM for the GEM-3 [9], again considering the aluminum and stainless-steel cylinders addressed above. We utilize the resonant

19

frequencies from Figs. 2 and 3 to perform a least-squares fit of the resonant modes to the frequency-domain EMI data. In these computations we consider the $m=0$ modes (no azimuthal variation of the currents induced in and on the target). The results in Fig. 6 correspond to the aluminum target, while the results in Fig. 7 are for the stainless-steel target. We see that a single pole does a reasonable job of fitting the frequency-dependent EMI data, while an excellent fit is obtained using two modes (poles 1 and 2 from Figs. 2 and 3).
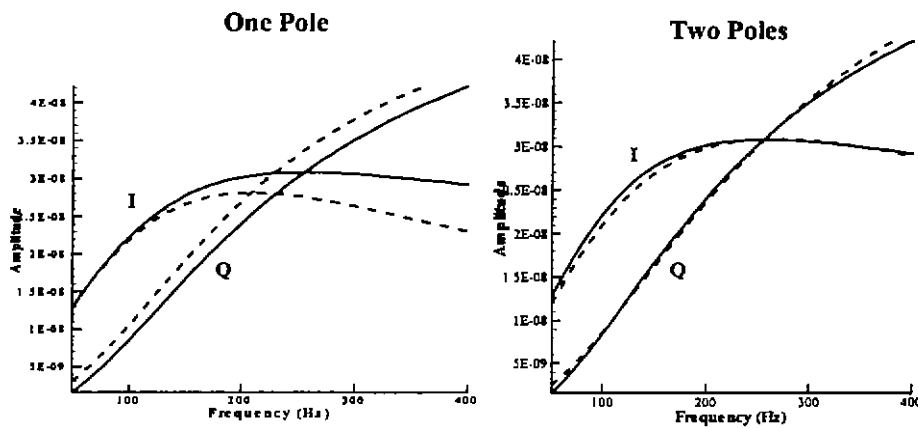
One Pole   **Two Poles**

Figure 6. Frequency-dependent EMI response of a 1-inch diameter, 1-inch high aluminum cylinder. The solid lines correspond to the MoM-computed EMI response for the GEM-3 sensor, and the dashed lines represent the least-square fit to the data, using one (left) and two (right) resonant poles.
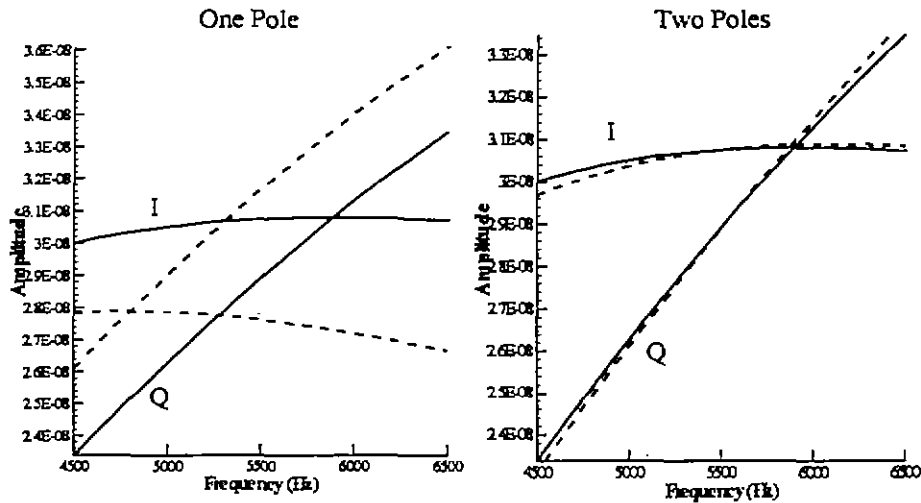
Figure 7. As in Fig. 6, but for a stainless-steel cylinder.

The results in Figs. 6 and 7 indicate that, when the set of resonant modes is consistent with the data under test, a very good least-squares fit can be obtained between the data and a modal representation. However, for discrimination to be effective, the least-squares fit should be poor when the data under test is inconsistent with the considered, *i.e.*, when poles from Target A are used to try to fit data from Target B. Considering the aluminum and stainless-steel targets investigated above, one would expect this to be the case, given the disparate characteristics of the associated target resonances. To examine this issue, in Fig. 8 we show frequency-domain EMI data from the stainless-steel disk, as fitted to resonances from the aluminum target of the same geometry. We see that this fit is very poor, indicating the utility of this technique for target discrimination.
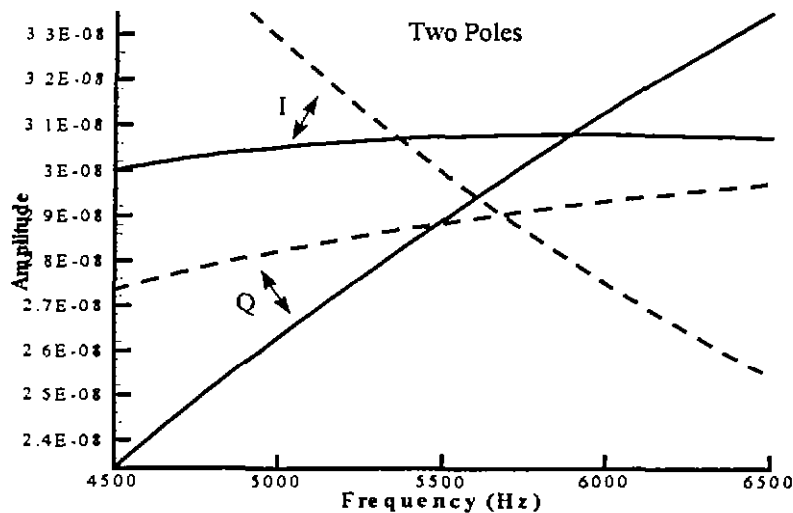
21

Figure 8. Frequency-dependent EMI response of a stainless-steel cylinder (solid curves), and the fit of this data to a linear combination of the first two principal poles of an aluminum cylinder (dashed curves). The dimensions of the two targets are identical.

C. Dependence of EMI response on target-sensor orientation

All of the results in Figs. 6-8 were for the GEM-3 coils [9] aligned such that their axis was coincident with the axis of the targets. Since we are interested in discriminating concealed (buried) targets, the target-sensor orientation is in general unknown. It is therefore of interest to examine the modal representation of the frequency-dependent EMI response when the target and sensor are *not* axially aligned. In Figs. 9 and 10 we consider the EMI response for the GEM-3 placed 15 cm above the target, with the GEM-3 and target centers offset by radial distance 0, 10, 20 and 25 centimeters, for the stainless-steel cylindrical target. Here we again use the principal two $m=0$ modes(for $cos(m\phi)$ azimuthal variation), with which we see an excellent fit to the frequency-dependent data. This implies that, despite the fact that the sensor and target are offset with regard to one another, the induced currents in the target are largely independent of the azimuthal direction on the target. For larger targets we may require higher-order modes ($m>0$) to achieve a satisfactory match between the measured data and the least-squares fit, when the target and sensor are offset (due to asymmetric induced currents).
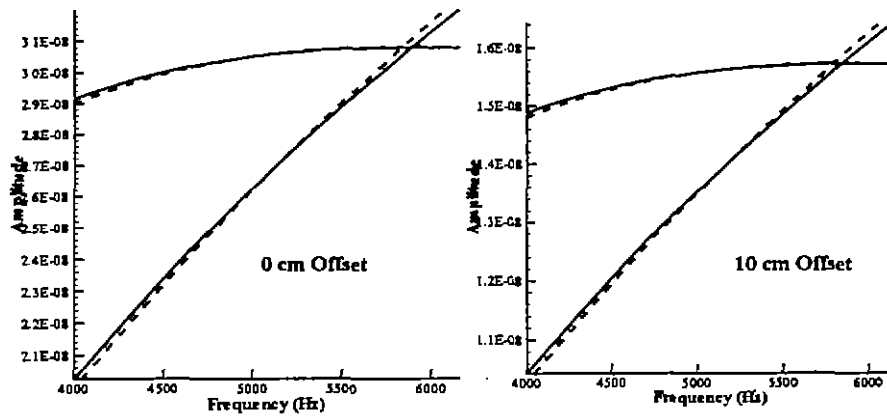
22

Figure 9. EMI response of a 1-inch diameter, 1-inch high stainless steel cylinder, as seen by the GEM-3 system. The solid curves represent the I and Q scattered response, computed via MoM, and the dashed curves represent the least-square fit using the principal two $m=0$ resonant modes for this target. The target and sensor axes are offset by 0 (left) and 10 cm (right).
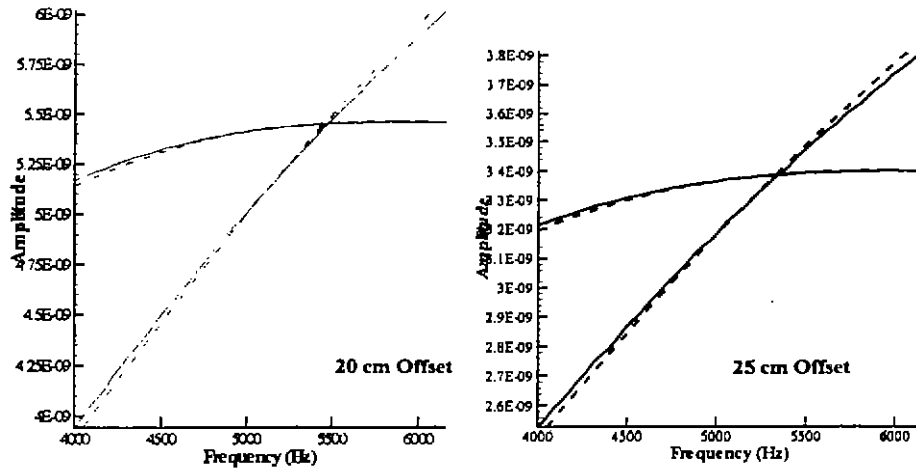
Figure 10. As in Fig. 9, for offsets of 20 and 25 centimeters.

Before leaving the issue of target-sensor orientation, we note that the different $m=0$ resonant modes characteristic of a particular cylindrical target differ only in the radial dependence of the induced currents. Consequently, one might anticipate that the excitation strengths of the various $m=0$ modes from a given target would be affected (approximately) in the same manner as the target-sensor orientation is changed. If this were the case, the *relative* strengths of the various $m=0$ modes would be *independent* of the target-sensor orientation. Therefore, there is only a *single* aspect-dependent parameter needed to describe the frequency-dependence of the EMI response [21]. In other words, for the cases considered above, for which two modes were sufficient to characterize the EMI response, the ratio b_1/b_2 should be approximately independent of target-sensor orientation. As discussed below, similar issues hold if more than two $m=0$ modes are required. This property significantly reduces the number of parameters we must compute, and by constraining the ratio b_1/b_2, we further match the modal expansion to the target of interest (we reduce the number of free parameters).

24

To test this hypothesis, in Table 1 we plot the ratio b_1/b_2 for the stainless-steel target, when the sensor is placed 15 cm above the target, and the radial offset between the GEM-3 coils [9] and the target axis are 0, 10, 20 and 25 cm. We see that, for all target-sensor orientations considered, b_1/b_2 is approximately 1.70. This is an important property that can be exploited in the context of discrimination.

Offset (cm)	Ratio b_1/b_2
0	1.746
10	1.767
20	1.719
25	1.670

Table 1. Ratio of modal amplitude of stainless-steel target, as a function of target-sensor offset.

The above discussion implies that the relative excitation strengths of the EMI resonances are aspect independent. This is because each has the same azimuthal variation. However, if $m=1$ modes were excited, the relative strength of excitation for the $m=0$ and $m=1$ modes *will be* aspect dependent. However, the relative strength of the $m=1$ modes, with respect to each other, will again be aspect independent [21].

VI. Statistical Analysis of Time-Domain and Frequency-Domain EMI

A. Theory

Assume that the vector $f=[f_1 f_2 \dots f_N]^T$ is representative of the N discrete, *real* samples from a given measurement, where the superscript T represents the transpose vector operation. In the

context of wideband electromagnetic induction (EMI), these numbers could represent N time-domain samples used to represent the measured exponential decay from a buried conducting target, while in the context of wideband frequency-domain EMI, this can represent the in-phase (I) and quadrature (Q) components measured at $N/2$ frequencies, the in-phase component at N frequencies, or the quadrature component at N frequencies. In each case, we assume that the signal f is corrupted by additive white Gaussian noise (WGN). Hence, if $s=[s_1\ s_2\ ...\ s_N]^T$ represents the response of the target in the absence of noise, $f=s+n$, where $n=[n_1\ n_2\ ...\ n_N]^T$ is WGN. The objective is to use the measured signal f, and implicitly the underlying target response s, to identify the target, with this process complicated by the additive noise n. It is assumed that the noise-free response s is known, from either measurement or theoretical model. Moreover, we assume that there are M signatures $s_1, s_2, ... s_M$ available, representative of the M targets to be identified or distinguished.

Under the aforementioned circumstances, optimal target discrimination [20] is effected by considering the M random variables $v_m=s_m^T f$, where f is a noisy waveform measured from a target to be identified, as described above. We assume the signals s_m have been normalized. The numbers v_m are random, as a consequence of the additive system noise n, and under the above assumptions we declare f representative of target k if $|v_k| \geq |v_m|\ \forall\ m \in [1, 2, ..., M]$. The purpose of the present study is an analysis of the statistical performance of such a identification procedure, for time-domain and frequency-domain EMI systems. Further, with regard to the latter scenario, we examine performance as a function of bandwidth. To perform the above discrimination paradigm, we require knowledge of the signals s_m. For time-domain operation, this assumes knowledge of the late-time decay constants, which can be computed or measured. For frequency-domain operation, it requires knowledge of the relative excitation strength of each resonant mode, for a particular target. As discussed with regard to Table 1, this is often approximately aspect independent.

Within this paradigm, we must consider the statistical properties of the M random variables v_m that are calculated when attempting to identify the target from the measured waveform f. The assumption that n is WGN implies that the random variables v_m are also distributed in a Gaussian manner. In particular, the mean of v_m, represented by the expectation $E(v_m)$, is given by

$E(v_m)=E(s_m{}^Tf)=s_m{}^Ts$, where $f=s+n$ (*i.e.*, the measured data f is characteristic of a target with noise-free response s, where it is assumed that s is one of the aforementioned s_1, s_2, ... s_M). If noise n is uncorrelated with variance σ^2 ($E(n_i n_k)=\sigma^2\delta_{ik}$, where the Kronecker delta $\delta_{ik}=1$ if $i=k$, and $\delta_{ik}=0$ otherwise), then the v_m are correlated in a simple manner. In particular, we define the M-dimensional vector $\underline{v}=[v_1\ v_2\ ...\ v_M]$, which is computed by performing inner products of the measured data f with the library of expected target signatures s_1, s_2, ... s_M. The vector v is described by the *correlated* Gaussian distribution

$$p(v) = [(2\pi)^M \det C]^{1/2} \exp[-\frac{1}{2}(v-m)^T C^{-1}(v-m)] \tag{16}$$

where $m=[m_1\ m_2\ ...\ m_N]^T$, $m_k=E(v_k)=E(s_k{}^Tf)=s_k{}^Ts$, and C is the M×M covariance matrix, defined as $C=E(vv^T)$. One can readily show that the C_{ik}, representative of the ik-component of the matrix C, is given by $C_{ik}=\sigma^2\ s_i{}^Ts_k$. With the statistics of v defined in (16), we can now predict the statistical properties of the *optimal* EMI discrimination algorithm discussed above.

Assume that the target considered in the measurement f is represented by the signal s_1 (*i.e.*, "target 1"). In this case, proper classification occurs if $|v_1|>|v_2|$, $|v_1|>|v_3|$, ..., $|v_1|>|v_M|$. The probability that this occurs is defined as the probability of proper classification, P_c. Using (16), we can explicitly compute P_c as [20]

$$P_c = \int_{-\infty}^{\infty} dv_1 \int_{-|v_1|}^{|v_1|} d v_2 \int_{-|v_1|}^{|v_1|} d v_3 \cdots \int_{-|v_1|}^{|v_1|} d v_M\ [(2\pi)^M \det C]^{1/2} \exp[-\frac{1}{2}(v-m)^T C^{-1}(v-m)] \tag{17}$$

The integrals in (17) cannot be evaluated analytically, and therefore are computed here via numerical integration.

27

B. Example results

We utilize the results from (17) to consider the relative efficacy of wideband time-domain and frequency-domain EMI. We consider conducting spheres of 1 inch diameter, composed of aluminum and brass, and address the ability of an EMI system to discriminate these targets. This issue can be addressed for more than just two targets, but the integration in (17) becomes more time consuming. Aluminum and brass are selected because these targets have similar conductivities, and therefore this poses are relatively difficult case. We have shown experimentally and theoretically [6] that the principal EMI modes of these targets have "resonant" frequencies of f_a=j260 and f_b=j651, respectively, for the aluminum and brass target.

As we have discussed previously, the frequency-domain EMI transfer function $H(f)$ for a conducting target is expressed as

$$H(f) = b \frac{f}{f - f_r} \tag{18}$$

where b is an amplitude constant and f_r represents the (imaginary) resonant frequency. In (18) we assume that only a single principal mode is of importance. The real part of $H(f)$ is called the in-phase (I) component, while the imaginary part is termed the quadrature (Q) component. In the time domain, the corresponding impulse response is expressed as

$$h(t) = -b2\pi \mid f_r \mid e^{-2\pi f_r t} \tag{19}$$

In the test we consider, we assume that the data in (18) or (19) is sampled, at a frequency sampling rate Δf or temporal sampling rate Δt. Moreover, we assume that the library of target signatures s_1, s_2, ... s_M are normalized (here we consider M=2), i.e., $s_m^T s_m$=1. The data under

28

consideration is shown in Figs. 11 and 12, in the time and frequency domain, respectively. The time-domain data corresponds to 64 data samples at Δt=0.1 msec, where the frequency-domain data corresponds to 50 samples, at Δf=20 Hz. As discussed, we consider measured data f=s+n, and the signal-to-noise ratio is defined as $s^T s/\sigma^2$, where σ^2 is again the noise variance.
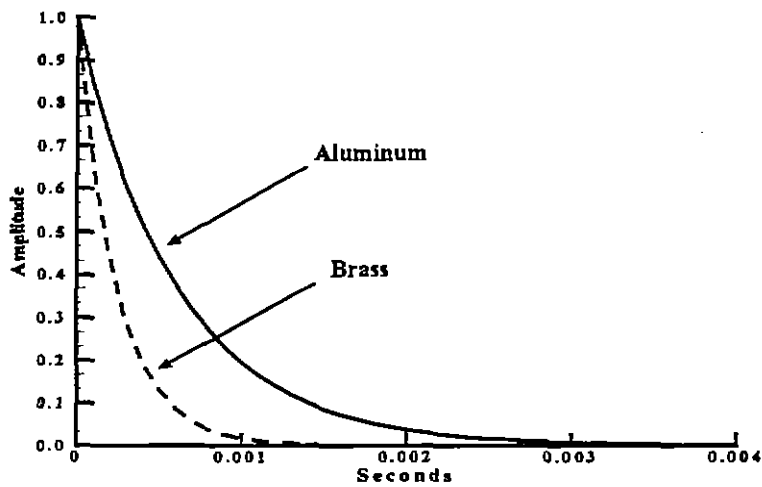

Figure 11. Late-time EMI response of aluminum and brass spheres, of 1-inch diameter.
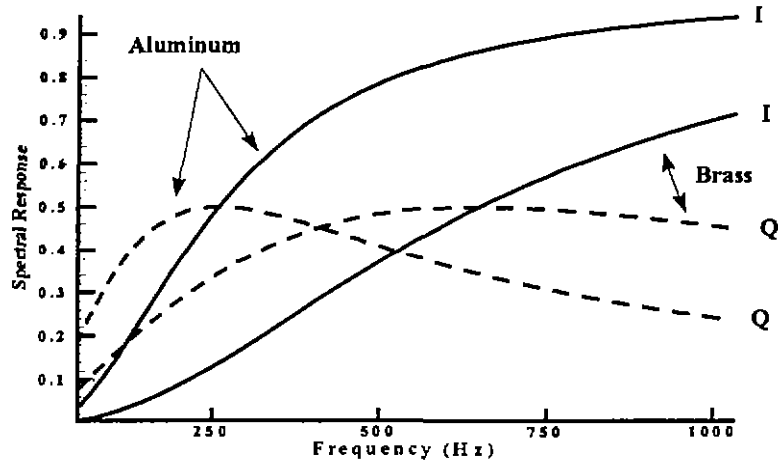
29

Figure 12. Frequency-domain EMI response for the two targets considered in Fig. 11.

In Fig. 13 we plot the probability of correctly distinguishing the aluminum target from its brass counterpart, plotted as a function of SNR. The results were computed using a bandwidth of 1 KHz, which from Fig. 12 is sufficient to capture the principal features of the targets' transfer functions. By taking Fourier transforms of the signals in Fig. 11, it is clear that the late-time transient responses contain principal frequencies less than approximately 1 KHz. If the time- and frequency-domain contain the same bandwidth and the same noise levels, time- and frequency-domain performance are identical.
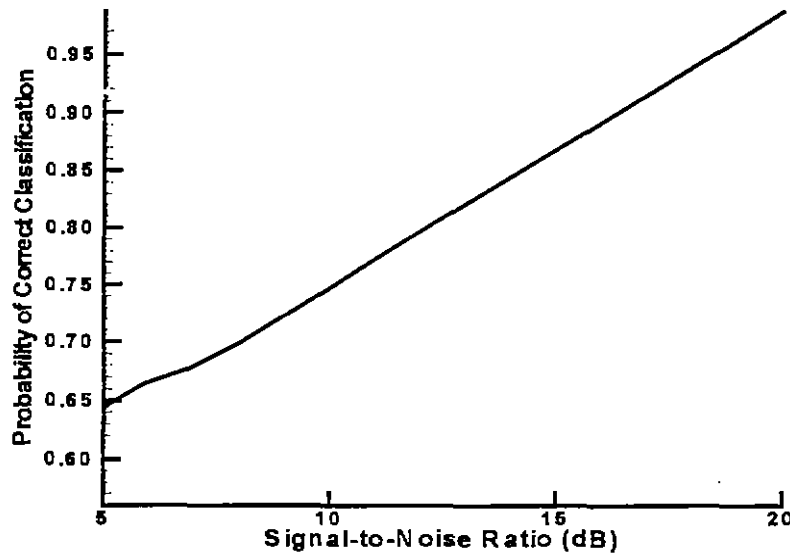
Figure 13. Probability of correctly distinguishing an aluminum from a brass 1-inch sphere. These results are for either frequency- or time-domain operation, assuming that the temporal and frequency-domain sampling are such that the signal energy and noise characteristics are the same in the two domains.

A very important point must be made while interpreting the results in Fig. 13. In a time-domain EMI system, one can only use the late-time portion of the signal to effect the above target discrimination. This implies that we only process such data for time $t > T$, where T is the nominal temporal extent of the driven EMI response (*i.e.*, the temporal duration of the source). It is well known that for small conducting targets, often over 95% of the time-domain signal energy occurs at $t < T$, and therefore the late-time response is quite small in amplitude. By contrast, a frequency-domain system need not distinguish early and late times, since steady-state measurements are being acquired. Consequently, *all* of the EMI energy is exploited in a frequency-domain EMI system. Therefore, returning to Fig. 13, recall that the SNR is defined as $s^T s / \sigma^2$. In a frequency-domain system $s^T s$ corresponds to *all* of the scattered energy, while for time-domain processing $s^T s$ corresponds to the much smaller late-time signature, for $t > T$ only. Thus, if σ_f and σ_t correspond to the noise variance of a frequency- and time-domain system, respectively, then we require $\sigma_t \ll \sigma_f$ such that the frequency-

31

and time-domain systems achieve the same SNR. In other words, a time-domain system must operate with a noise variance which is much smaller than that of a frequency-domain system if the two are to achieve equal performance. This suggests that a frequency-domain system is most appropriate for discrimination of relatively small targets.
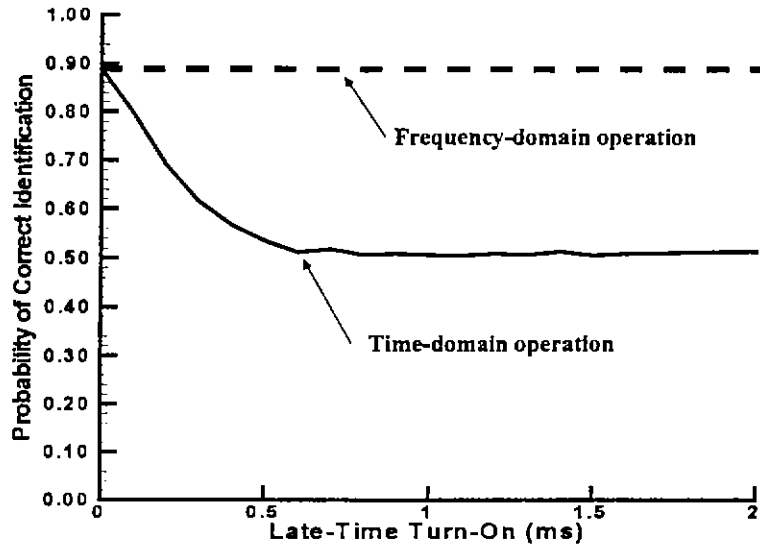

Figure 14. Probability of correctly identifying aluminum and brass 1-inch spheres, using a frequency- and time-domain EMI system. With regard to the time-domain case, we plot results as a function of the turn-on time T, and resonance-based transient EMI identification is performed for t>T. The frequency-domain scheme implicitly exploits both early- and late-time information, and therefore it is independent of T. Results are plotted for the 15 dB SNR case in Fig. 13 (the noise variance is held constant, and therefore the actual time-domain SNR decreases with increasing T, since the late-time energy decreases as T increases).

To demonstrate this, in Fig. 14 we plot the performance of a time- and frequency-domain EMI system, for distinguishing the aluminum and brass 1-inch spheres. In these results the noise variance is chosen as that characteristic of the 15 dB SNR data in Fig. 13. Recall that for time-domain EMI processing we only utilize time t>T, where T is the nominal duration of the excitation.

Consequently, if the noise variance and excitation strength are held constant, as T increases we are implicitly processing a late-time time-domain scattered waveform that has been further damped and therefore is more undermined by noise. For a frequency-domain system, the discrimination performance is independent of T. The results in Fig. 14 demonstrate dramatically that, for the (small) targets considered, a frequency-domain system is superior than its time-domain counterpart, since T is always greater than zero. For a time-domain system with 2 KHz bandwidth, T is approximately 0.5 ms. For a time-domain system to operate with the same quality as a frequency-domain system, the bandwidth must be increased markedly such that the turn-on time T is as small as possible (relative to the decay rate of the damped exponential).

As we have discussed in Sec. IVB, large and/or highly ferrous targets have corresponding resonant frequencies that are too small to be encompassed within the system bandwidth of most practical frequency-domain EMI systems. Further, we have found that a frequency-domain system provides poor discrimination when the target resonant frequencies are too small to be encompassed within the system bandwidth. For example, in Sec. IVB we demonstrated that large and/or ferrous targets often have resonant frequencies f_r less than 1 Hz. For such targets, it is virtually impossible to build a frequency-domain system with bandwidth that encloses f_r. Consequently, a frequency-domain system is most appropriate for small targets, while a time-domain system is optimal for large and/or ferrous targets. This motivates a hybrid frequency-domain/time-domain system for applications involving both large and small targets, as well as ferrous and non-ferrous.

VI. Conclusions

A detailed study of frequency- and time-domain EMI has been undertaken. It has been demonstrated that both the frequency-domain and time-domain signatures can be parametrized entirely in terms of the low-frequency EMI resonances, with such characterized by nearly purely imaginary frequencies. This recognition significantly simplifies target discrimination, for the characteristic target signatures can be expressed compactly in terms of a few parameters. We also

33

demonstrated that useful properties exist with regard to the relative excitation strengths of multiple resonant modes. Finally, we have undertaken a detailed analysis of the efficacy of frequency- and time-domain EMI sensing, in the presence of additive system noise. Assume $j\omega_r$ represents the principal resonant frequency of the target in question. If ω_r is within the bandwidth of a frequency-domain EMI system, frequency-domain sensing is efficacious. However, large and/or ferrous targets are often characterized by very small ω_r, too small to be within the bandwidth of a practical frequency-domain EMI system. A small ω_r implies a slow resonant decay for a time-domain system, implying that such targets are best interrogated with a time-domain EMI sensor. Summarizing, this study indicates that an optimal EMI sensor will operate in both the frequency and time domains, with the former appropriate for smaller targets and the latter best suited to larger and/or ferrous targets.

References

[1] D. Kajfez and P. Guillon (eds.) *Dielectric Resonators*, pp. 259-325, Artech House, Dedham, MA, 1986

[2] C.E. Baum, "Low-frequency near-field magnetic scattering from highly, but not perfectly conducting bodies," Interaction Note 499, Nov. 1993; Ch. 6, p. 163-218, in C.E. Baum, in (Ed. C.E. Baum), *Detection and Identification of Visually Obscured Targets*, Taylor & Francis, 1998.

[3] C.E. Baum, N. Geng and L. Carin, "Integral equations and polarizability for magnetic singularity identification," Interaction Note 524, March 1997.

[4] G.D. Sower, Eddy current responses of canonical metallic targets – theory and measurements," Interaction Note 526, May 1997.

[5] L.S. Riggs, J.E. Mooney, D.E. Lawrence, J.T. Broach, and A.H. Trang, "On identifying conducting objects using low frequency magnetic fields- theory and measurement," Interaction Note 542, July 1998.

[6] N. Geng, C.E. Baum, L. Carin, "On the low-frequency natural response of conducting and permeable targets," IEEE Trans. Geosc. Remote Sens. Jan. 1999.

[7] C. A. Balanis, *Advanced Engineering Electromagnetics*, John Wiley & Sons, 1989.

[8] R. F. Harrington, *Field Computation by Moment Methods*, The Macmillan Company, New York, 1968

[9] I. J. Won, D. A. Keiswetter, D. R. Hanson, "GEM-3: A Monostatic Broadband Electromagnetic Induction Sensor," *J. Environmental Engineering Geophysics*, vol. 2, pp. 53-64, March 1997

[10] M. G. Andreasen, "Scattering from Bodies of Revolution," *IEEE Trans. Ant. and Prop.*, vol. 13, pp. 303-310, March 1965

[11] J. R. Mautz, R. F. Harrington, "Radiation and Scattering from Bodies of Revolution," *Appl. Sci. Res.*, vol. 20, pp. 405-435, June 1969

[12] S. D. Gedney, R. Mittra, "The use of the FFT for the efficient solution of the problem of

electromagnetic scattering by a body of revolution," *IEEE Trans. Ant. and Prop.*, vol. 38, pp. 313-322, March 1990

[13] S. Vitebskiy, K. Sturgess, L. Carin, "Short-pulse plane-wave scattering from buried perfectly conducting bodies of revolution," *IEEE Trans. Ant. and Prop.*, vol. 44, pp. 143-151, Feb. 1996

[14] T. Wu, L. L. Tsai, "Scattering from arbitrarily-shaped lossy dielectric bodies of revolution," *Radio Science*, vol. 12, pp. 709-718, Sept.-Oct. 1977

[15] J. R. Mautz, R. F. Harrington, "Electromagnetic scattering from a homogeneous material body of revolution," *AEÜ*, vol. 33, pp. 71-80, Feb. 1979

[16] A. W. Glisson, D. R. Wilton, "Simple and efficient numerical methods for problems of electromagnetic radiation and scattering from surfaces," *IEEE Trans. Ant. and Prop.*, vol. 28, pp. 593-603, Sept. 1980

[17] A. W. Glisson, D. Kajfez, J. James, "Evaluation of modes in dielectric resonators using a surface integral equation formulation," *IEEE Trans. Micr. Theory and Techn.*, vol. 31, pp. 1023-1029, Dec. 1983

[18] A. W. Glisson, "Integral Equation Techniques," in *Dielectric Resonators*, ed. D. Kajfez and P. Guillon, pp. 259-325, Artech House, Dedham, MA, 1986

[19] D. Kajfez, A. W. Glisson, J. James, "Computed modal field distributions for isolated dielectric resonators," *IEEE Trans. Micr. Theory and Techn.*, vol. 32, pp. 1609-1616, Dec. 1984.

[20] H.L. VanTrees, *Detection, Estimation, and Modulation Theory*, Wiley, 1968.

[21] S.M. Kay, *Fundamentals of Statistical Signal Processing*, Prentice Hall, 1993.

[22] C.E. Baum, "Use of residue and constant-dyadic information in magnetic singularity identification," Interaction Note 547, Aug. 1998.